PHYSICAL REVIEW E **81**, 016401 (2010)

Density and potential profiles of non-neutral electron plasmas in a magnetic mirror field

H. Higaki, K. Fukata, K. Ito, and H. Okamoto
Advanced Sciences of Matter, Hiroshima University, 1-3-1 Kagamiyama, Higashi-Hiroshima, Hiroshima 739-8530, Japan

K. Gomberoff
Physics Department, Technion, Haifa 32000, Israel

(Received 30 June 2009; published 7 January 2010)

Low-energy non-neutral electron plasmas were confined with an electrostatic potential and a magnetic mirror field of the mirror ratio up to 5. Using a conventional phosphor screen and the unique multiring trap, both radial and axial density profiles of plasmas were measured. With the present experimental parameters, it was confirmed that a plasma density increased at higher field with an electrostatic confinement and that it decreased at higher field with a magnetic mirror confinement. The electrostatic potentials along the magnetic field were estimated with computer simulations.

DOI: 10.1103/PhysRevE.81.016401 PACS number(s): 52.27.Jt, 52.55.Jd, 52.65.Rr

I. INTRODUCTION

A wide variety of plasmas have been studied in a magnetic mirror field. For example, high-ion-energy quasineutral plasmas are confined in a magnetic mirror field for nuclear fusion research, plasmas with high-energy electrons in electron cyclotron resonance ion sources produce highly charged ions for physics research, a low-density large scale space plasma can be observed in the earth's magnetosphere, etc. Also, it is known that low-energy non-neutral plasmas play crucial roles for the production and confinement of a large number of antihydrogen atoms in a special magnetic mirror field [1,2]. Since a magnetic mirror can confine both positive and negative charged particles simultaneously, it may provide a chance to study low-energy electron-positron plasmas experimentally [3]. Thus, it must be important to understand the basic properties of non-neutral plasmas in a magnetic mirror field.

So far, low-energy non-neutral plasmas have been confined in various apparatuses and their properties have been investigated both theoretically and experimentally [4]. Although there have been some theoretical works [5,6] and simulation studies [7,8], little experiment has been performed for a low-energy non-neutral plasma confined with a simple magnetic mirror field. Therefore, basic properties such as confinement times, radial density profiles, and electrostatic plasma oscillations have been studied recently [9]. In the previous report, low-energy non-neutral electron plasmas were confined by an axis symmetric magnetic mirror field on one side and by an electrostatic field on the other side. This is possible because the radial particle diffusion and the axial particle loss at the electrostatic potential are negligible compared to those at the magnetic mirror field.

Here, employing a conventional imaging system composed of a phosphor screen (PS) and a charge coupled device (CCD) camera, a radial density profile measurement becomes much easier than the previous report. This makes the axial density profile measurement possible with the use of a multiring trap which has a lot of electrodes along the magnetic mirror filed. When an electrostatic potential is also applied at high-field side, non-neutral plasmas confined electrostatically on both sides in a magnetic mirror field can be studied. Obtained experimental results are compared to numerical results by a particle in cell (PIC) simulation named WARP.

II. EXPERIMENTAL SETUP

Shown in Fig. 1(a) are examples of a measured magnetic field along the axis of symmetry and an electrostatic potential applied to ring electrodes. A magnetic mirror field was produced by two series of magnetic coils. For example, keeping a current of coils on the low-field side I_L fixed to 10 A, which produced the field of about 33G, a current of the other coils on the high-field side I_H could be increased from 10 to 80 A. In the present experiment, it corresponded to the mirror ratio $R \sim 5$. Here, the mirror ratio is defined as $R = B_{max}/B_{min}$, where B_{min} is the minimum magnetic field at $z \sim 0$ cm and B_{max} is the maximum field at $z \sim 70$ cm in the confinement region.

For applying the electrostatic potential, a multiring electrode trap [9–11] was aligned along the axis of symmetry as schematically shown in Fig. 1(b). The trap contained 45 ring electrodes with inner diameter of 7 cm and thickness of 1.2 cm. They were separated by 1.6 cm each in the axial direction from −6.7 to 63.7 cm. With these electrodes, the trap was very flexible in applying the electrostatic potential. Four consecutive electrodes at low-field side from −6.7 to −1.9 cm were used to provide the axial confinement of electrons with an electrostatic potential $V_L = -30$ V, as denoted by the thin solid line in Fig. 1(a). Another set of electrodes at high-field side from 58.9 to 63.7 cm was used to supply electrostatic voltage $V_H \sim -12$ V to confine a large number of electrons at the beginning of an experiment. The vacuum pressure in a series of experiments reported here was less than 1×10^{-8} torr.

Electrons were provided by an electron gun installed on the axis of symmetry at $z \sim 98$ cm. It means that electrons were injected from the high-field side. A phosphor screen was placed on the low-field side at $z \sim -30$ cm so that a radial density distribution could be measured easily. Since the PS is aluminum coated (500 Å in thickness), it was also used as a Faraday cup when the total number of electrons N_e

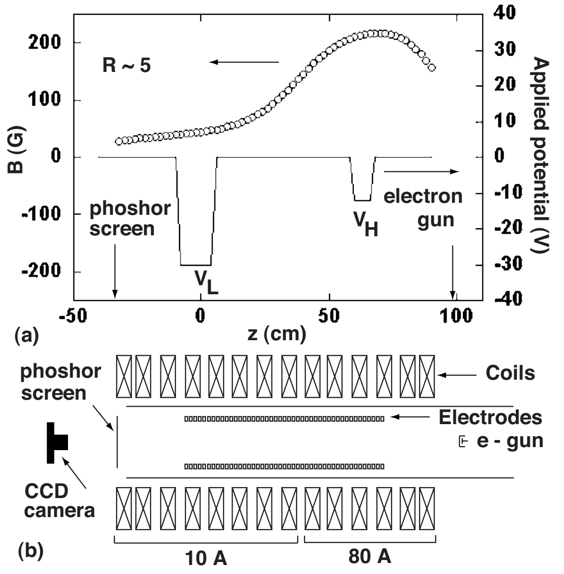

FIG. 1. (a) The basic configuration of an applied magnetic field and electrostatic potential. Open circles denote the measured magnetic field strength on the axis of symmetry when $I_L = 10$ A and $I_H = 80$ A. Thin solid line corresponds to the applied electrostatic potential. Arrows show the positions of an electron gun and a phosphor screen. (b) A schematic drawing of the experimental setup.

was to be measured electronically. Phosphor (P20) with a thickness of 15 μm and an effective diameter of 75 mm is mounted on a glass plate and biased to +8 kV when an axially integrated radial density profile was measured. A grounded mesh was also installed in front of PS to make the acceleration field almost parallel to the magnetic field. To obtain the images of PS when the electrons are dumped, a progressive scan CCD camera (480×640 pixel, 10 bit, monochrome) with a 12 mm fixed focal length lens was employed here. The electronic shutter speed was fixed to 1/30 s and controlled by the external trigger. Typically, 100 images were accumulated for a profile measurement to improve the signal-to-noise ratio.

The following procedure was employed in the experiments to reproduce the initial condition of trapped electrons. At first, electrons were injected and confined axially with electrostatic potentials on both ends. The number of electrons reached 10^9 at most. After 150 ms, the electrons were close to the local thermal equilibrium with the electron temperature $T_e \sim 1.0$ eV and the electron density n_e in the order of 10^6 cm^{-3}. The temperature T_e was estimated by measuring the axial electron energy distribution near the axis of symmetry with a retarding potential method. The corresponding Debye length λ_D became less than 0.7 cm. Then the electrostatic potential V_H at high-field side was grounded to start a magnetic mirror confinement. After holding electrons for 5 ms, the electrostatic potential V_L in front of PS at low-field side was grounded for measurement. When axial density profiles are measured, the potential of $V_{cut} = -50$ V was applied to a ring electrode 200 μs before V_L was grounded. Then, a confined plasma was divided into two parts at the position of the ring electrode and only a plasma at low-field side was dumped to PS for a profile measurement [12]. By changing a ring electrode where V_{cut} was applied, an axial density profile could be obtained effectively.

III. EXPERIMENTAL RESULTS

It should be noted that the axial profile measurement was performed for three types of plasmas. The first one was a plasma confined with electrostatic potentials on both sides of a magnetic mirror. This is referred to as an electrostatic confinement in this paper. Shown in Fig. 2(a) is an example of a 100 shots averaged image of such a plasma. The color gradient is normalized to its peak intensity. Since the local intensity is proportional to the local area density of electrons, a radial intensity distribution reflects a radial electron distribution. Here, unit intensity corresponds to about 100 electrons per pixel or 4.4×10^5 electrons per cm^2. The area density is obviously an integration of electrons along a curved magnetic field.

The second one was a plasma confined with a magnetic mirror field at high-field side and an electrostatic field at low-field side and it had a hollow profile as reported previously [9]. Figure 2(b) shows an image of a plasma with a hollow profile. The third one was confined in the same way as the second one. However, it had a bell-shaped profile like the first one as shown in Fig. 2(c). Although this profile is intuitively obvious, it seems that there is no theoretical model for a bell-shaped profile in a magnetic mirror confinement. Both the second and the third ones are referred to as a magnetic mirror confinement here. Since $\lambda_D (\leq 2$ cm) is longer in case of the magnetic mirror confinement, it may be ambiguous if these are called plasmas in radial direction. At least these are plasmas in axial direction because the axial electrostatic oscillations are observed for both electrostatic and magnetic mirror confinements.

For each type of plasmas, the radial intensity profile was measured by applying V_{cut} to 11 electrodes (at $z = 8.0$, 12.8, 17.6, 22.4, 27.2, 32.0, 36.8, 41.6, 46.4, 51.2, and 56.0 cm). Shown in Figs. 2(d)–2(f) are parts of the cross sections of intensity profiles for the corresponding plasmas [Figs. 2(a)–2(c)]. Each color, light blue, pink, black, green, and blue, denotes the cross section of intensity profiles when V_{cut} was applied to the electrodes at $z = 12.8$, 22.4, 32.0, 41.6, and 51.2 cm, respectively. Total intensity profiles (red line) are also plotted as a function of radial position. In these figures, one pixel corresponds to ~ 0.15 mm.

With the measured intensity profiles, the normalized axial intensity distribution $I_n(z)$ can be deduced as follows. The Debye length $\lambda_D \sim 0.7$ cm for electrostatically confined plasma is much smaller compared to the axial extent of the plasma of ~ 60 cm. However, it clearly causes the diffuse boundary in radial direction as seen in Fig. 2(d). Also, in case of magnetic mirror confinements, a smaller density results in longer $\lambda_D \leq 2$ cm. Thus, the intensity profile near the axis of symmetry, where the intensity becomes almost flat, was used to plot the normalized axial intensity as a function of z. The normalized intensities $I_n(z)$ in Figs. 2(g)–2(i) are obtained by averaging the intensity within the radius of 30 pixels from the axis of symmetry and normalizing the averaged intensity with the one from the total profile (red lines).

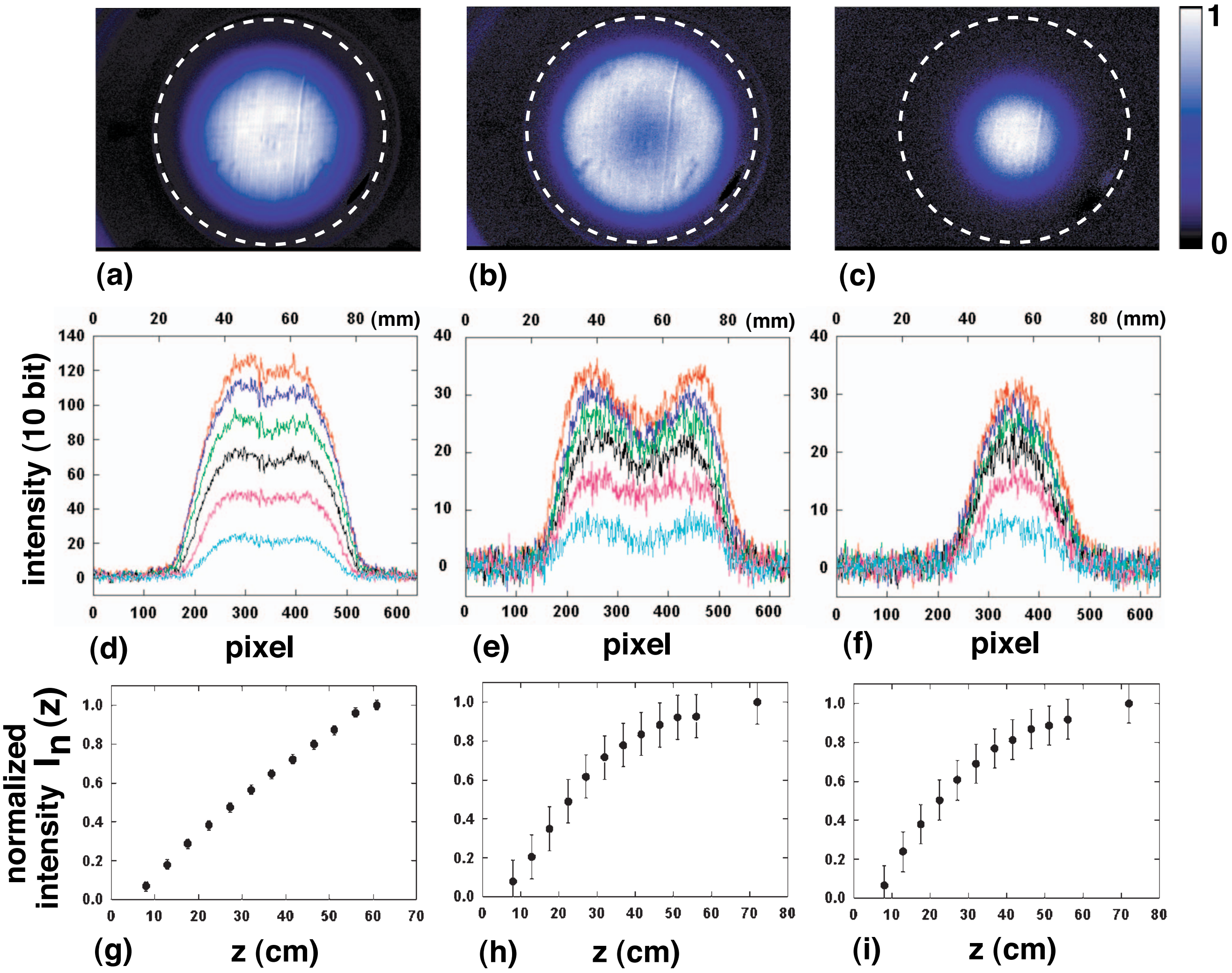

FIG. 2. (Color) Examples of obtained images, radial density profiles, and axial distributions when $R \sim 3$. (a) Image for the electrostatic confinement. (b) Image for the magnetic mirror confinement with a hollow profile. (c) Image for the magnetic mirror confinement with a bell-shaped profile. White dashed lines show the area of the phosphor screen. (d)–(f) show cross sections of corresponding images. Each color represents a different axial position where V_{cut} was applied. (g)–(i) show normalized intensity $I_n(z)$ along the axis of symmetry.

A differentiation of $I_n(z)$ by z tells how an axial electron number depends on z in the magnetic-flux tube.

Qualitatively, it is seen from Fig. 2(g) that there are almost equal number of electrons along the fixed magnetic-flux tube near the axis of symmetry in case of electrostatic confinement. Since the area of the flux tube becomes smaller at higher field, the experimental results suggest that the electron density becomes higher at high-field side, as expected previously [6,12]. On the other hand, in case of magnetic mirror confinement, the number of electrons clearly decreased at higher magnetic field as shown in Figs. 2(h) and 2(i). It is necessary to consider the change of the magnetic field strength to deduce the electron density along the axis.

Before proceeding to the evaluation of the electron density, similar axial intensity profiles are measured and plotted in Fig. 3 for mirror ratios $R \sim 1-5$. The results shown in Figs. 3(a) and 3(b) are for the electrostatic confinement and the magnetic mirror confinement, respectively. As for the solid circles in Fig. 3(a), each color, orange, blue, green, black, and red, represent the data with $R \sim 1$, 2, 3, 4, and 5. In Fig. 3(b), color notations are the same and the solid circles and open squares denote data for hollow profiles and bell shaped profiles. It is seen that there is no clear dependence on the radial profiles for the magnetic mirror confinement. In case of electrostatic confinement with $R \sim 1$, the intensity profile can be fitted nicely with a linear function as shown by the solid orange line in Fig. 3(a). This means that the electron density is almost constant along the uniform magnetic field. Since the cross section of the linear fitting at horizontal axis was $z \sim 5.2$ cm, all the data in Fig. 3 are shifted by 5.2 cm for the easiness of fittings and the horizontal axes are denoted by $Z = z - 5.2$.

Then, the second and third order polynomial functions are used to fit the data for the electrostatic confinements and the magnetic mirror confinements. Normalized electron number as a function of position Z can be obtained by differentiating the fitting curves. As mentioned above, when an axial density distribution along the magnetic field near the axis of symmetry is evaluated, the change of the magnetic field strength along the axis should be considered. Since the magnetic field

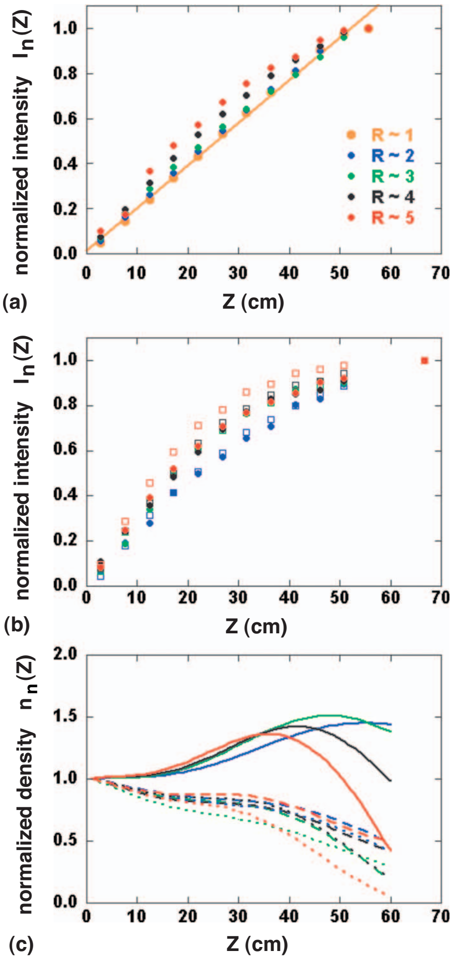

FIG. 3. (Color) Normalized axial intensity distributions with various R for (a) electrostatic confinement and (b) magnetic mirror confinement, respectively. It is seen that the axial distribution becomes linear for the uniform magnetic field ($R \sim 1$). (c) Normalized axial electron densities near the axis of symmetry are evaluated with the measured magnetic field strength and plotted as a function of position.

strength $B(Z)$ on the axis of symmetry was measured for each R used in the experiments, it was used to evaluate a local electron density of a plasma along the magnetic field. Here, the normalized electron density $n_n(Z)$ was calculated by the following equation, where $S(Z) \equiv B(0)S(0)/B(Z)$ denotes the area of the magnetic-flux tube under consideration:

$$n_n(Z) = \frac{dI_n(Z)/dZ}{S(Z)} \Bigg/ \frac{dI_n(0)/dZ}{S(0)} = \frac{dI_n(Z)/dZ}{dI_n(0)/dZ}\frac{B(Z)}{B(0)}. \quad (1)$$

Obtained normalized electron densities $n_n(Z)$ are summarized in Fig. 3(c) for both electrostatic confinements (solid lines) and magnetic mirror confinements (dashed lines and dotted lines). Dashed lines are for the hollow profiles and dotted lines are for the bell-shaped profiles, respectively. Color notations are the same as before. It is clearly seen that the electron density becomes higher up to a certain density at high-field side in case of electrostatic confinements. Although experimental errors are large for the magnetic mirror confinements, it is seen that the electron density decreased at higher magnetic field.

According to the Boltzmann relation, the fact that the plasma density changes along a magnetic field in an equilibrium state suggests that the electrostatic potential is created along the magnetic field [6,12]. However, it is difficult to measure the potential in present experiments. To obtain some practical insights into the potential profile along the magnetic field, it is better to confirm the experimental results with a particle simulation including real experimental parameters. It will be also useful because an electrostatic potential along a magnetic mirror field is expected to play an important role for the production of low-energy electron-positron plasma in a magnetic mirror field and antihydrogen atoms in a cusp field.

IV. SIMULATION RESULTS AND DISCUSSIONS

A. Simulation method

In order to study equilibrium states in the electrostatic and magnetic mirror confinements, the method developed for the numerical modeling of a non-neutral plasma equilibrium in a trap with high magnetic field is adopted. Details of the method have been reported elsewhere [13]. It was applied to study a theoretical equilibrium state in a trap with a simple magnetic mirror field [7] and to study a plasma in an antihydrogen trap with multipole magnetic fields [8]. The theoretical model studied the behavior of a non-neutral plasma in a trap with a magnetic mirror field in which the field changed only in a small restricted region [6]. The analytical results were confirmed with the numerical method. For example, it was shown that the potential and density are not constant along magnetic field lines allowing the trapping of particles not only in the low-field region but also in the high-field region. The simulation results for the antihydrogen trap were consistent with the experimental results that followed [1]. Therefore, the method is capable of finding unknown plasma evolution and an equilibrium state of a plasma under complex trap configurations with realistic three-dimensional (3D) fields.

To study equilibrium states in such traps, the collisionless PIC code WARP [14] was employed. In the simulation method [13], the inherent numerical collisionality was exploited as the source for the relaxation to an equilibrium state. Among the advantages of WARP is the capability of simulating the different drifts and Larmor radius without resolving the gyromotion in time or in space [15]. The fact that a simulation time step can be longer than the gyroperiod made it possible to simulate relatively long processes in large geometries, as is the case here, while the necessary small time step with other codes would result in unreasonable calculation time. Another advantage is the steerable compatibility of WARP which permits, for example, turning on the magnetic mirror field gradually and adding simulation particles gradually.

Here, the same method [13] was applied to the present experimental setup to find the equilibrium states of a plasma in a magnetic mirror field with and without the electrostatic potential V_H at high field. These correspond to the equilib-

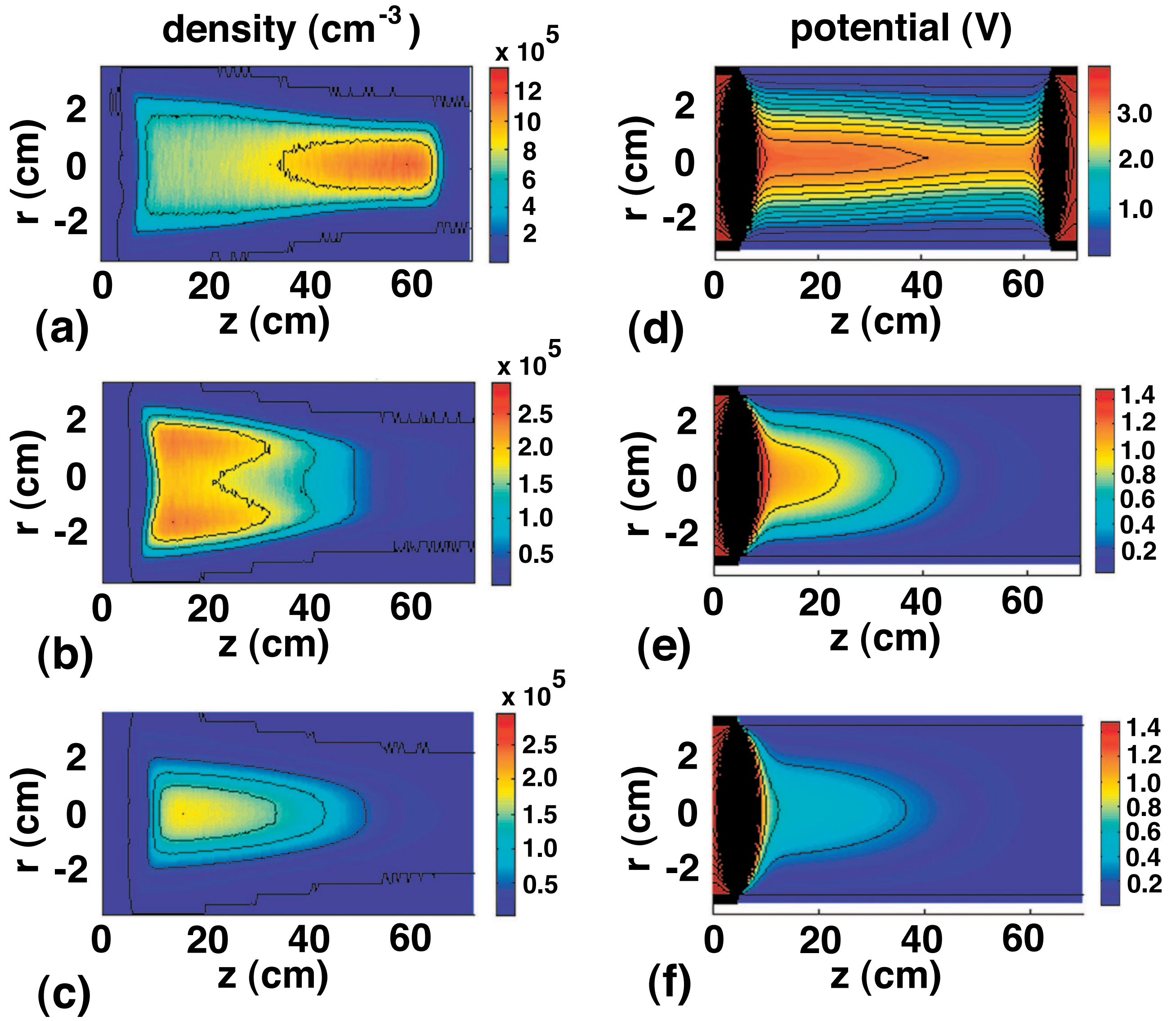

FIG. 4. (Color) Calculated density and potential distributions of plasmas with the magnetic mirror field $R \sim 3$. (a) The density distribution in the electrostatic confinement with $r_0 = 2$ cm has a higher density at high field. (b) In the magnetic mirror confinement with $r_0 = 2$ cm, a hollow profile is observed with the higher density at low field. (c) With a smaller radius of $r_0 = 1$ cm in the magnetic mirror confinement, a bell-shaped profile is reproduced. Electrostatic potentials corresponding to (a), (b), and (c) are shown in (d), (e), and (f), respectively

rium states in an electrostatic confinement and in a magnetic mirror confinement, respectively. Initially, the plasma is loaded with an ideal local equilibrium found with another code [16]. The other code solves an equilibrium of the plasma inside a trap with two ring electrodes in a uniform axial magnetic field. The Boltzmann distribution along a constant radius is assumed and the Poisson equation is solved. Since the equilibrium along a field line is considered, there is freedom to choose a radial density profile. For most simulations here, a top-hat distribution (a constant density) was used. A smooth distribution can be also used as an initial density profile.

Then, a PIC simulation starts under a uniform magnetic field with the magnitude at the low-field region. When the loaded ideal equilibrium becomes stable in computation, the remaining mirror field is ramped slowly over a few tens of μs. The ramping time should be slow compared to other significant physical processes. Those include the gyroperiod ($\sim 10^{-9}$ s), plasma oscillation period ($\sim 10^{-7}$ s), transit time $\sim 10^{-6}$ s, and $E \times B$ drift ($\leq 10^{-5}$ s). The time step is 10^{-8} s, which is larger than the gyroperiod. When the solution is stabilized, an equilibrium state for the electrostatic confinement is obtained. Then, the potential V_H is gradually decreased (in the same time scale with the field ramping time) until it is grounded. After some simulation time, an equilibrium state for a magnetic mirror confinement is obtained.

B. Simulation results

In Fig. 4, contour plots of the plasma densities and potentials are shown for three cases with $R \sim 3$. Plasma densities in Figs. 4(a)–4(c) are calculated for plasmas in an electrostatic confinement with an initial radius of $r_0 = 2$ cm, a magnetic mirror confinement with $r_0 = 2$ cm, and a magnetic mirror confinement with $r_0=1$ cm, respectively. These plasmas correspond to those in Fig. 2. As expected, a plasma has the higher density at high-field region in the electrostatic confinement [Fig. 4(a)]. In case of magnetic mirror confinements, simulations reproduced the experimental results, i.e., a larger initial plasma radius resulted in a hollow profile and a small initial plasma radius resulted in a bell-shaped profile. It is inferred that there is a critical radius, where the equilibrium profile changes from a hollow one to a bell-shaped one depending on the initial plasma density, temperature, profile, mirror ratio, and so on. When a smooth radial profile was used as an initial profile in simulation, it was observed that a density gradient in hollow profile was emphasized. The details of the parameter dependence will be studied more in the future.

Shown in Figs. 4(d)–4(f) are the calculated plasma potentials corresponding to Figs. 4(a)–4(c), respectively. It should be noted that the sign of the potential is inverted for the clarity. In Fig. 4(d), the potential difference inside the plasma along the axis $\Delta\phi \sim 0.5$ V is observed for the electrostatic confinement where a magnetic mirror field changes smoothly in the long axial range. It was expected [6] that this $\Delta\phi$ in the present experiment with a smooth magnetic mirror field should be almost the same with the one calculated previously for the analytical model [7]. An interesting point is that $\Delta\phi$ along the axis in case of the magnetic mirror confinement as in Fig. 4(e) could be lager than that of electrostatic confinement.

Considering the fact that the loss cone boundary of the magnetic mirror trap is modified due to the presence of electrostatic potential [3,7], the hollow profile is reasonable. Because the larger $\Delta\phi$ near the axis results in the smaller confinement region in the velocity space and the smaller $\Delta\phi$ at the larger radius means the larger confinement region and results in a larger number of trapped particles. It is also thought that fractions of particles at high-field region redistribute themselves along the field line at a larger radius, when V_H is grounded and the particles near the axis escape the trap at first. The fraction of particles remained inside the trap contributes to the higher density at larger radius in magnetic mirror confinement. The bell-shaped profile with the similar potential distribution might mean that $\Delta\phi$ is smaller than the plasma temperature.

For the purpose of investigating the effect of density profiles on $\Delta\phi$, ramping the magnetic field and grounding the potential V_H were conducted simultaneously. It is referred to as the simultaneous ramping process. It could be performed only in simulations. In experiments, the magnetic field was kept constant in time. During the simultaneous ramping process, less particles were contained at high field as shown in Fig. 5(a), which should be compared to the density distribution in Fig. 4(a). It leads to less particles at larger radius in the magnetic mirror confinement. Shown in Fig. 5(b) is the resultant density distribution with $R\sim 3$ and $r_0=2$ cm, which is closer to a bell-shaped profile compared to Fig. 4(b). Thus, the final equilibrium state depends on how the magnetic mirror confinement is achieved.

Simulations were also performed for an electrostatic confinement and a magnetic mirror confinement with $R\sim 5$ and $r_0=2$ cm. When R becomes larger, the density and potential gradients in both the electrostatic confinement and the magnetic mirror confinement become larger.

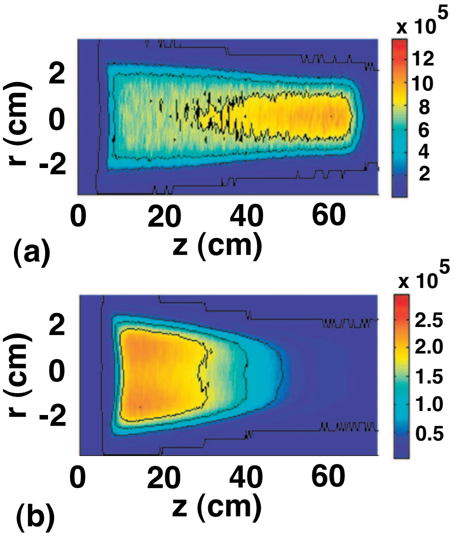

FIG. 5. (Color) (a) A density distribution during the simultaneous ramping of the magnetic mirror field and grounding of the potential V_H. (b) A density distribution in the magnetic mirror confinement with $R\sim 3$ obtained with the simultaneous ramping process. Compared to Fig. 4(b), the density distribution is closer to a bell-shaped one.

The density and potential along the axis of symmetry are plotted in Fig. 6. Figure 6(a) shows the axial density for various cases discussed above. Solid lines are for electrostatic confinements and dashed lines are for magnetic mirror confinements. Dot-dashed lines in Fig. 6(a) are the initial densities in a uniform magnetic field at the beginning of PIC simulations. The color notations are provided in Fig. 6. The normalized axial densities in Fig. 6(b) correspond to the experimental results shown in Fig. 3(c). Although Fig. 6(b) agrees qualitatively with Fig. 3(c), there are a few differences. For example, the position of the maximum density stays near B_{max} in simulations, while in experiments it moves toward the lower field for larger R. The curvatures of density gradients are different. Also, it was found in the simulation that 20% of initial particles were left in the magnetic mirror confinement with $R\sim 3$ and $r_0=2$ cm, while in experiment, 33% of initial particles were left. This is partly because the density profiles and scattering processes of trapped particles in simulations are not exactly the same with those in experiments. In experiments, electrons are scattered by each other and by background neutral particles while in simulations, particles are scattered by numerical collisionality.

Despite of all the differences, simulations reproduced experimental results as a whole. Thus, the simulation results can provide approximate electrostatic potentials. Shown in Fig. 6(c) are the potentials along the axis of symmetry calculated for various cases. The potential difference for $R\sim 5$ becomes as large as $\Delta\phi \sim 1.4$ V in magnetic mirror confinement with $r_0=2$ cm. The smallest $\Delta\phi$ is for the plasma with $R\sim 3$ and $r_0=1$ cm in the electrostatic confinement. It is also seen that $\Delta\phi$ for the electrostatic confinements is less than 0.5 V. With the present experimental conditions, it is thought that a larger $\Delta\phi$ is achieved for the magnetic mirror confinement.

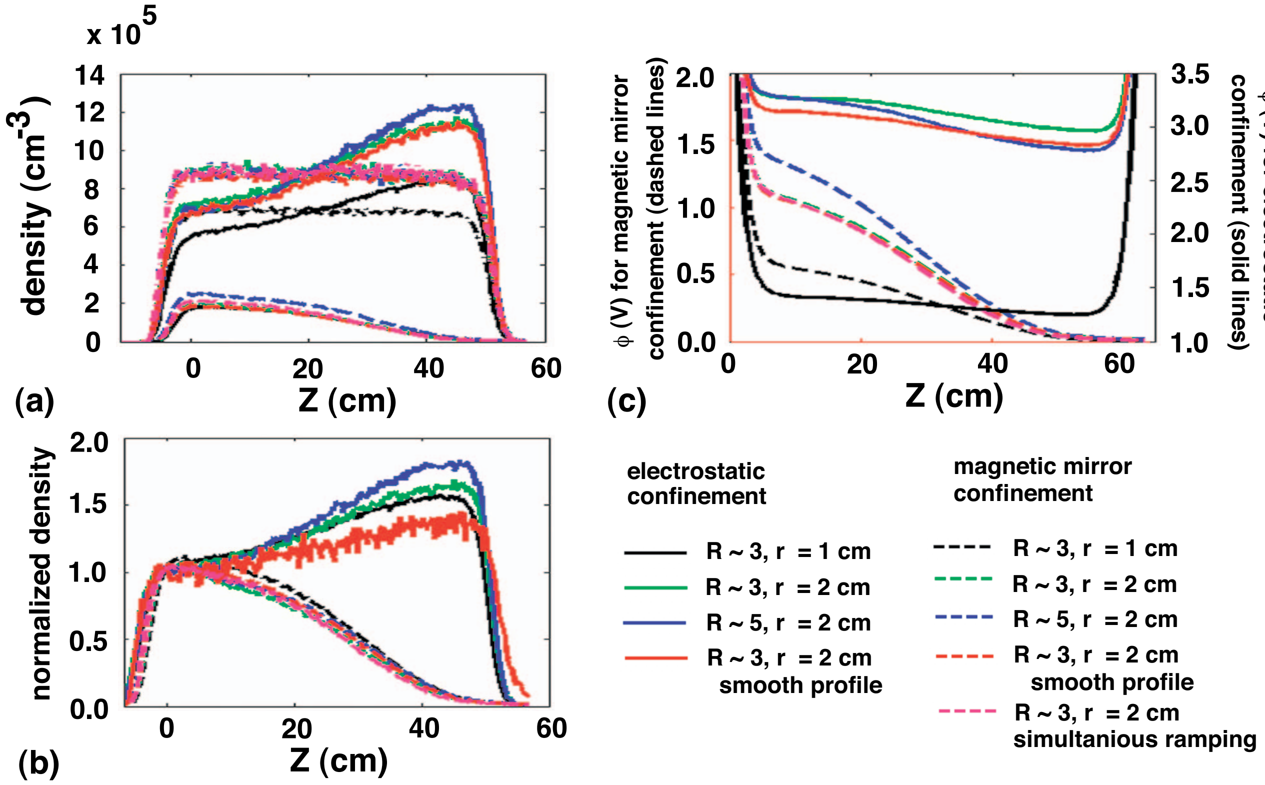

FIG. 6. (Color) (a) Calculated density distributions along the axis of symmetry. Dash-dotted lines are the distributions in a uniform magnetic field at the beginning of simulation. (b) Normalized density distributions along the axis of symmetry, which should be compared to those in Fig. 3(c). (c) Electrostatic potentials along the axis of symmetry. It is seen that $\Delta\phi$ in magnetic mirror confinement (dashed lines) are larger than those in electrostatic confinement (solid lines).

The dashed magenta line for the simultaneous ramping process shows the potential for the bell-shaped profile with $R\sim 3$ and $r_0=2$ cm. It has almost the same potential profile with that for the hollow profile ($R\sim 3$, $r_0=2$ cm). The smooth profile with $R\sim 3$ and $r_0=2$ cm also has the similar potential profile. Therefore, $\Delta\phi$ does not depend on the radial density profile so much. It seems that $\Delta\phi$ depends on the total number of particles and axial density profile in both electrostatic and magnetic mirror confinements.

It should be noted that the potential is created so that the oppositely charged particles can be confined at the lower magnetic field. Although the potential difference is small due to the limited number of confined electrons and small density, it is expected that the potential difference along the magnetic field line will be useful for confining low-energy positrons inside a non-neutral electron plasma in a magnetic mirror field.

V. SUMMARY

Low-energy non-neutral electron plasmas were confined with a magnetic mirror field of the mirror ratio R up to 5 to investigate both radial and axial density distributions inside the magnetic mirror fields. Not only a hollow profile but also a bell-shaped profile was found to be stable as a radial density profile for a non-neutral plasma in a magnetic mirror field. It was confirmed experimentally that a plasma density increased at higher field with an electrostatic confinement and that it decreased at higher field with a magnetic mirror confinement. Potential differences along the magnetic field line were evaluated with a PIC code WARP. Although the calculated potential difference was in the order of ~ 1 V, it will be useful for the production of a low-energy electron-positron plasma in a magnetic mirror field. The obtained results suggest that a small magnetic mirror trap with a potential plugging outside the magnetic mirror will be the easiest way to produce low-energy electron-positron plasmas.

ACKNOWLEDGMENTS

This work is partly supported by a Grant-in-Aid for Scientific Research from the Ministry of Education, Culture, Sports, Science, and Technology (Grant No. 20540483), the 2008 Hiroshima University Fujii Research Promotion Fund, and Israel Science Foundation (Grant No. 1080/06).

[1] G. Andresen *et al.*, Phys. Rev. Lett. **98**, 023402 (2007).

[2] J. Fajans, W. Bertsche, K. Burke, S. F. Chapman, and D. P. van der Werf, Phys. Rev. Lett. **95**, 155001 (2005).

[3] H. Higaki, in *Cold Antimatter Plasmas and Application to Fundamental Physics*, edited by Y. Kanai and Y. Yamazaki, AIP Conf. Proc. No. 1037 (AIP, Melville, NY, 2008), p. 106.

[4] *Non-Neutral Plasma Physics VI*, edited by M. Drewsen, U. Uggerhoj, and H. Knudsen, AIP Conf. Proc. No. 862 (AIP, Melville, NY, 2006), p. 176.

[5] R. C. Davidson, A. T. Drobot, and C. A. Kapetanakos, Phys. Fluids **16**, 2199 (1973).

[6] J. Fajans, Phys. Plasmas **10**, 1209 (2003).

[7] K. Gomberoff, J. Fajans, J. Wurtele, A. Friedman, D. P. Grote, R. H. Cohen, and J.-L. Vay, Phys. Plasmas **14**, 052107 (2007).

[8] K. Gomberoff, J. Fajan, A. Friedman, D. P. Grote, J.-L. Vay, and J. Wurtele, Phys. Plasmas **14**, 102111 (2007).

[9] H. Higaki, K. Ito, W. Saiki, Y. Omori, and H. Okamoto, Phys. Rev. E **75**, 066401 (2007).

[10] H. Higaki and A. Mohri, Jpn. J. Appl. Phys. **36**, 5300 (1997).

[11] A. Mohri, H. Higaki, H. Tanaka, Y. Yamazawa, M. Aoyagi, T. Yuyama, and T. Michishita, Jpn. J. Appl. Phys. **37**, 664 (1998).

[12] R. Gopalan, Ph.D. thesis, University of California, Berkeley, 1998.

[13] K. Gomberoff, J. Wurtele, A. Friedman, D. P. Grote, and J.-L. Vay, J. Comput. Phys. **225**, 1736 (2007).

[14] D. P. Grote, A. Friedman, J.-L. Vay, and I. Haber, in *Electron Cyclotron Resonance Ion Sources*, edited by M. Leitner, AIP Conf. Proc. No. 749 (AIP, Melville, NY, 2005), p. 55.

[15] R. H. Cohen, A. Friedman, M. Kireff Covo, S. M. Lund, A. W. Molvic, F. M. Bieniosek, P. A. Seidl, J.-L. Vay, P. Stolz, and S. Veitzer, Phys. Plasmas **12**, 056708 (2005).

[16] F. Peinetti, F. Peano, G. Coppa, and J. Wurtele, J. Comput. Phys. **218**, 102 (2006).